# The influence of depth-varying elastic properties of the upper plate on megathrust earthquake rupture dynamics and tsunamigenesis

Manel Prada[1], Percy Galvez[2], Jean-Paul Ampuero[3], Valenti Sallares[1], Carlos Sánchez-Linares[4], Jorge Macías[4], Daniel Peter[2]

[1]Barcelona Center for Subsurface Imaging, Institut de Ciències del Mar (ICM), Barcelona, Spain

[2]King Abdullah University of Science and Technology, Physical Science and Engineering Division, Saudi Arabia

[3]Université Côte d'Azur and Institut de Recherche pour le Développement, Nice, France

[4]EDANYA, Universidad de Malaga, Spain

## Abstract

Megathrust earthquakes are strongly influenced by the elastic properties of rocks surrounding the fault. However, these properties are often overestimated in numerical simulations, particularly in the shallow megathrust. Here we explore the influence that realistic depth-varying upper-plate elastic properties along the megathrust have on earthquake rupture dynamics and tsunamigenesis using 3D dynamic rupture and tsunami simulations. We compare results from three subduction zone scenarios with homogeneous and heterogeneous elastic media, and bimaterial fault. Elastic properties in the heterogeneous model follow a realistic depth-distribution derived from controlled-source tomography models of subduction zones. We assume the same friction properties for all scenarios. Simulations in the heterogeneous and homogeneous models show that rigidity variation of the country rock determines the depth-varying behavior of slip, slip rate, frequency content, and rupture time. Fault friction may provide additional constraints, but to a lesser extent. The depth-varying behavior of slip, frequency content, and rupture duration quantitatively agree with previous predictions based on worldwide data compilations, explaining the main depth-dependent traits of tsunami earthquakes and large shallow megathrust earthquakes. Large slip, slow rupture and slip rate amplification in bimaterial simulations are largely controlled by the elastic rock properties of the most compliant side of the fault, which in subduction zones is the upper plate. Large shallow slip and trenchward increasing upper-plate compliance of the heterogeneous model lead to the largest co-seismic seafloor deformation and tsunami amplitude. This highlights the importance of considering realistic variations in upper-plate rigidity to properly assess the tsunamigenic potential of megathrust earthquakes.

Key points:

We test the influence of realistic upper-plate rigidity on megathrust dynamic properties and tsunamigenesi using 3D numerical simulations

Simulations show that realistic upper-plate rigidity variations explain the depth-dependent behavior of earthquake dynamic properties

Overestimation of upper-plate rigidity leads to underestimation of co-seismic seafloor deformation and tsunami amplitude in our simulations.

# 1 Introduction

Megathrust earthquakes tend to nucleate within the seismogenic zone (Hyndman et al., 1997; Byrne et al., 1988). The updip limit of this region may vary depending on material properties and thermal conditions along the megathrust (Hyndman et al., 1997), but it is commonly defined between 5-10 km of depth (Scholz, 1998). Yet, megathrust earthquakes may occasionally rupture through the shallow and apparently aseismic region of the fault (< 5 km of depth), particularly in areas with sediment-starved trenches and irregular subducting topography (e.g. Polet and Kanamori, 2000; Geersen, 2019), and heterogeneous sediment thickness and elevated pore pressure (Tobin and Saffer, 2009; Li et al., 2018). When this occurs, the rupture produces anomalously large slip near the trench, dramatic seafloor deformation and large and devastating tsunamis. This is the case of tsunami earthquakes, which are defined as a particular type of shallow events that excite disproportionally large tsunamis for their moderate seismic magnitude (Kanamori, 1972). In addition, these are relatively slow earthquakes that radiate seismic waves depleted in high frequencies, which in turn leads to a large discrepancy between their surface-wave magnitude (Ms) and moment magnitude (Mw) (e.g. Kanamori and Kikuchi, 1993; Newman et al., 2011). However, an increasing number of observations demonstrate that these properties are not only particular of tsunami earthquakes, but of most shallow megathrust events, implying a depth-dependent behavior of megathrust earthquake rupture characteristics (Lay and Bilek, 2007; Lay et al., 2012). Large tsunamigenic earthquakes such as the 2004 Sumatra-Andaman (Mw9.2), 2010 Maule (Mw 8.8), and 2011 Tohoku-Oki (Mw 9.0) produced larger slip near the trench than at deeper portions of the fault (e.g. Lay et al., 2012). In addition, these large events displayed similar depth-dependent frequency content as tsunami earthquakes, with lower-frequeny energy mostly emanated from the shallow portion of the megathrust (e.g. Kanamori and Yomogida, 2011; Meng et al., 2011; Simons et al., 2011; Koper et a., 2012; Lay et al., 2012).

These seismological observations indicate that such depth-dependent behavior shares similarities between contrasting tectonic environments (erosional and accretionary margins) and earthquake sizes, suggesting the existence of a common contributing factor. The presence of low-rigidity subducting sediments has been invoked to explain some characteristics of shallow ruptures, in particular the large shallow slip and slow rupture (Bilek & Lay, 1999; Polet and Kanamori, 2000). However, numerical simulations show that the presence of a low velocity fault zone may result in acceleration of the rupture to supershear speed and produce high-frequency radiation (e.g. Huang and Ampuero, 2011; Huang et al., 2016), in contrast with seismological observations of shallow events (e.g. Kanamori and Kikuchi, 1993). On the other hand, results from numerical simulations explain the large slip and slow rupture observed in tsunami earthquakes with a large compliant sedimentary prisms and velocity-weakening fault friction conditions (Lotto et al., 2017). However, some tsunami earthquakes like the 1992 Nicaragua event occurred in erosional convergent margins with no accretionary prisms (McIntosh et al., 2007; Sallares et al., 2013), implying that the cause of large shallow slip and tsunamigenesis is controlled by factors other than well-developed sedimentary wedges. More recent research proposes that, rather than fault plane properties, the depth-varying behavior of earthquake properties, such as slip, rupture time, and frequency content may be explained by the distribution of elastic properties of rocks overlying the fault in the upper plate (Sallares & Ranero, 2019). Overall, all these studies share a common ground, in which the depth-varying behavior of earthquake properties is controlled by elastic properties of rocks involved in the rupture.

Over the last decade, there has been an increasing number of numerical studies attempting to understand the dynamics of megathrust earthquakes and their depth-varying behavior. Depth-dependent initial stress conditions and/or friction laws are invoked to explain the depth-varying behavior of the 2011 Tohoku-Oki event (e.g. Huang et al, 2012; Murphy et al., 2018), while other studies invoked inelastic wedge deformation to account for the depth-dependent behavior of tsunami earthquakes (Ma, 2012; Ma and Hirakawa, 2013). Yet, the distribution of elastic properties considered in most of these simulations tend to be homogeneous (e.g. Huang. et al. 2012), layered (e.g. Galvez et al., 2016), or constant for a given geological unit (e.g. Moreno et al., 2012; Murphy et al., 2018; van Zelst et al., 2019) and, in almost all cases, it is not extracted from data. This hinders understanding of the additional role that realistic elastic properties along the fault have on the dynamics of these events, and may lead to dynamic models in which fault friction is forced to explain most seismological observations. On the other hand, in some models, elastic properties of the shallow megathrust such as rigidity are considered one order of magnitude larger (e.g. Ma 2012) than estimated from drilling samples (Jeppson et al., 2018). The overestimation of elastic properties involved in the shallow rupture may lead to underestimation of slip, uplift and tsunami size (e.g. Satake, 1994; Geist and Bilek, 2001), thus underestimating related hazards.

Here, we use 3D numerical simulations to show that incorporating a realistic distribution of elastic properties has a first-order effect on the depth-dependent behavior of megathrust earthquakes and tsunamigenesis. We compare results from 3D dynamic rupture simulations obtained in two subduction zone scenarios with homogeneous and depth-dependent elastic properties, respectively, and we compare the outcomes in terms of slip, rupture duration, and frequency content. All scenarios share the same friction properties and fault geometry, so that any difference in rupture properties may be only attributed to differences in the elastic properties. We then explore the influence of bimaterial fault properties, in models that include the material contrast between the overriding and subducting plates. Finally, we assess the influence of depth-dependent rock rigidity on seafloor deformation and tsunamigenesis from tsunami simulations.

## 2 Dynamic rupture model setup

We consider a megathrust fault with a dip angle of 15º based on controlled-source tomographic models from the Middle American subduction zone (Sallares et al., 2013). We model three subduction scenarios: a homogeneous elastic medium, a heterogeneous medium, and a bimaterial fault. The values of P-wave velocity ($V_p$), S-wave velocity ($V_s$) and density ($\rho$) in the homogeneous medium are those of rocks of the overlying the megathrust at 20-25 km depth (Fig. 1d to 1g), while the heterogeneous medium includes a realistic depth-distribution of elastic properties inferred from worldwide controlled-source upper-plate tomographic models (Sallares and Ranero, 2019) (Fig. 1d to 1h). Depth variations in the heterogeneous model are not only due to changes in geological units (e.g. crystalline crust vs sediments), but may also reflect variations in the tectonic framework (e.g. density of fractures) within the same geological unit. This simplified representation of the heterogeneous distribution of elastic properties of the upper plate is consistent with first-order variations in which elastic moduli decrease towards the upper-plate toe (Fig. 1h) (Calahorrano et al., 2008; Sallares et al., 2013; Contreras-Reyes et al., 2017). This distribution of elastic properties is, therefore, ideal to explore how realistic elastic properties influence the rupture and the permanent upper-plate co-seismic deformation.

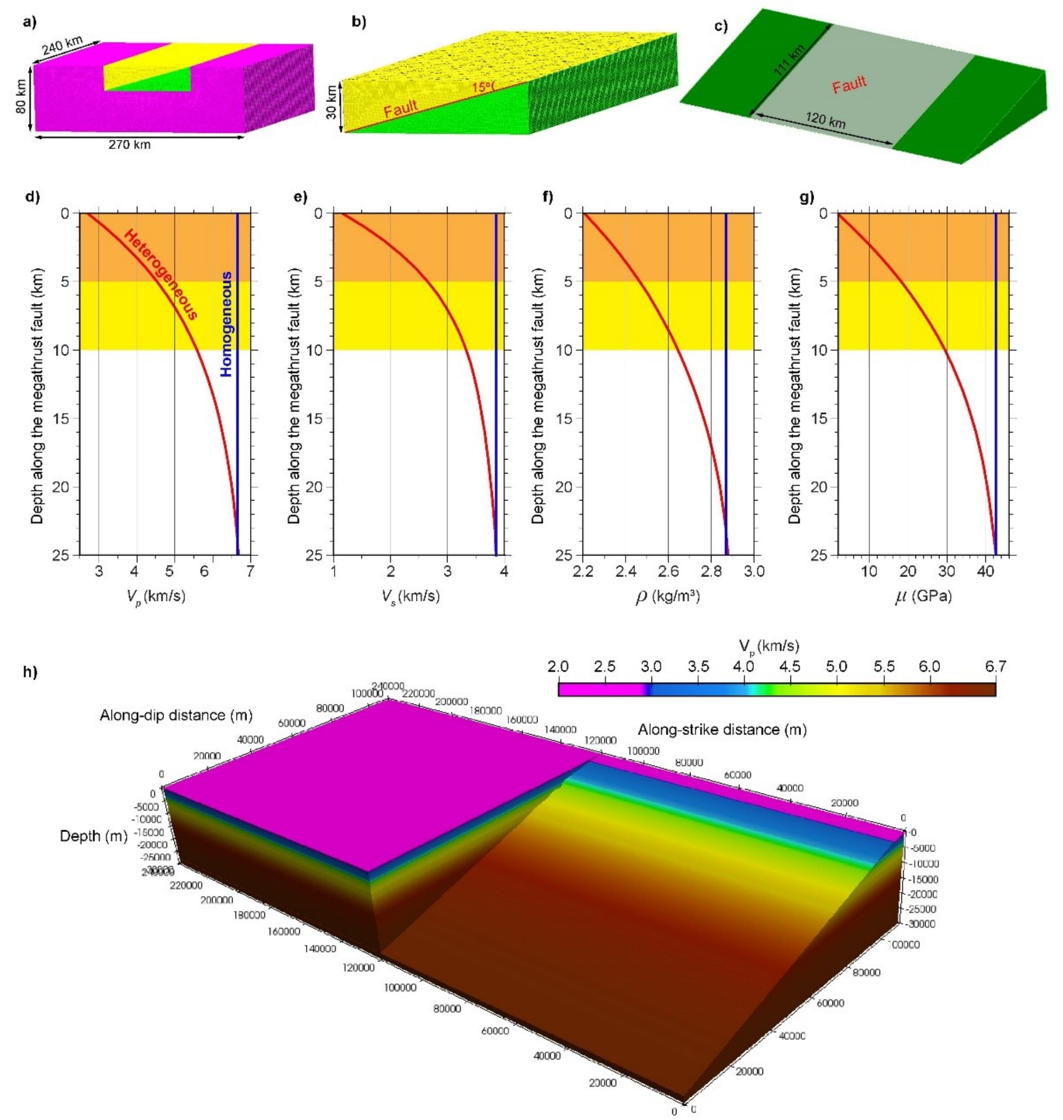


**Figure 1.-** a) Unstructured mesh showing the fault domain in b) and c) with 500 m element size. The rupture area of the fault is represented by the shaded area and is 120 wide and 111 km long. The fault dips 15º. Lower panels show the depth distribution of d) $V_p$, e) $V_s$, f) $\rho$, and g) rigidity ($\mu$) used in this study for the homogeneous (blue) and heterogeneous (red) models. Orange, yellow and white background color show the extent of the shallow, transitional, and regular domain, respectively. h) The same fault domain in b) showing the depth distribution of $V_p$-

We divide the fault in three different domains based on variation of elastic properties overlying the megathrust fault (Sallares and Ranero, 2019). This way, the “regular domain” extends from 30 to 10 km depth, the “transitional domain” from 10 to 5 km depth, and the “shallow domain” from 5 to 0 km depth (Fig. 1d to 1g). To capture the rupture properties characteristic of each domain, we performed three different sets of simulations, each confined to one of the three domains. We performed two simulations in each domain, one in the homogeneous medium and a second one in the heterogeneous medium.

For all simulations, we assume a linear slip-weakening friction law, with constant critical slip-weakening distance (Dc) of 0.4 m, static friction coefficient ($\mu_s$) of 0.6 and dynamic friction coefficient ($\mu_d$) of 0.4. The initial normal ($\sigma_n$) and shear stresses ($\tau_0$) are 100 MPa and 50 MPa, respectively, through the regular domain, and decrease linearly across the transitional and shallow domains to 10 MPa and 5 MPa at the surface, respectively (Fig. 2a to 2c). We run simulations in which the rupture is confined to a particular domain of the fault by setting $\mu_s$ to $10^4$ outside of it, strengthening the fault and preventing the rupture from propagating further. The rectangular nucleation zone in each domain was set as a region where initial shear stress exceeds initial shear strength in each domain, and its size was estimated to be large enough to sustain rupture propagation (Day et al 2005) (Figs. 2a to 2c). The nucleation patches are located at 24 km, 9 km, and 4.5 km of fault depth, for the simulations through the regular, transitional and shallow domains, respectively (Fig. 2a to 2c).

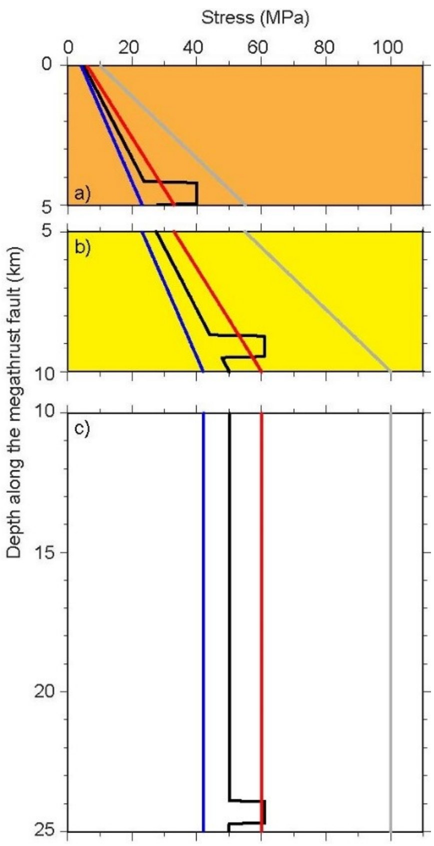


**Figure 2.-** Frictional parameters and nucleation zones for the a) shallow, b) transitional, and c) regular domains extracted from a cross section along the center of the fault. The blue line is the initial dynamic shear stress, black is initial shear stress, red curve is the initial shear strength, and gray curve is the initial normal stress.

To solve the dynamic rupture problem we use the open-source spectral element code SPECFEM3D (Peter et al., 2011) and its dynamic rupture capabilities (Kaneko, et al., 2008; Galvez et al., 2014). The simulations use an unstructured mesh generated with software CUBIT (Fig. 1). The mesh is 240 km wide, 270 km long and 80 km deep (Fig. 1a). The fault domain is a confined volume at the center of the mesh that extends over the first 30 km of depth, and is 240 km wide and 270 km long, although our models only rupture a square patch in the center of the fault that is 120 km wide and ~110 km long (Fig. 1b to 1c). The spectral element size in the fault domain is 500 m with 5 Gauss-Lobatto-Legendre (GLL) nodes per element edge, yielding an average grid size of 125 m, while outside the fault domain the element size gradually increases to 1 km at the boundaries of the mesh.

# 3 Numerical Results

We simulated ruptures confined to each of the three fault domains, as well as whole-depth ruptures. The results in the heterogeneous medium show clear depth-varying values of slip, source duration, frequency content, rupture speed, and slip rate, in contrast to simulations in homogeneous medium.

## 3.1 Slip

Figure 3 shows the spatial distribution of slip ratio between the heterogeneous and homogeneous models ($Slip_{het}/Slip_{hom}$) through each of the three domains (absolute values are shown in Figure S1). In all fault domains, the rupture through the heterogeneous model results in larger slip than in the homogeneous (Fig. 3); particularly in the shallowmost 5 km of the fault (i.e. shallow domain), where the slip ratio increases from 3 to 9 as we approach the trench (Fig. 3). Despite these slip differences, similar moment magnitudes are obtained in both elastic models in the shallow (Mw~7.5), transitional (Mw ~7.5), and regular domains (Mw ~ 8.4) as we are using the same rupture surface ($S$) and stress drop ($\Delta\tau$) in both simulations, and

$$M_o = \Delta\tau \, S^{3/2} \, C^{-1}, (3)$$

where $M_o$ is seismic moment and $C$ is a geometric constant of order one.

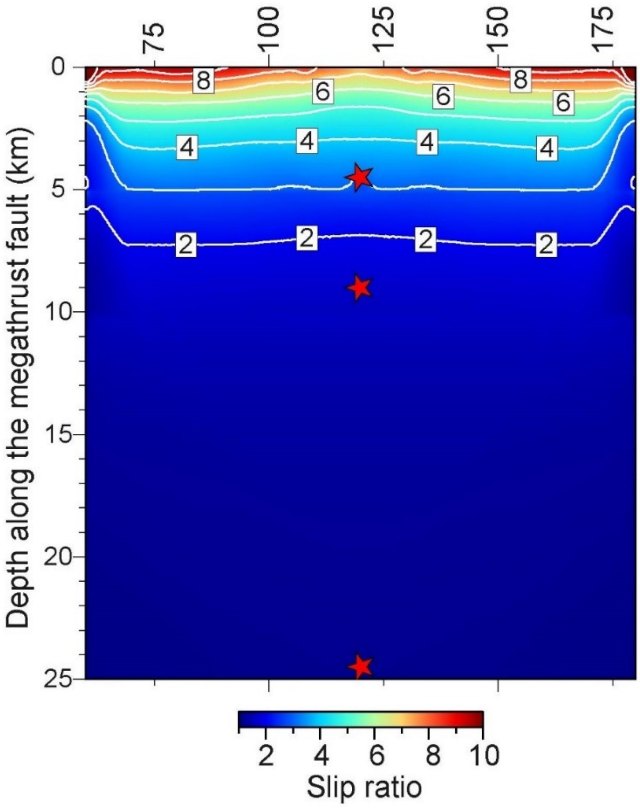


**Figure 3.-** Slip ratio (Slip $_{het}$/Slip $_{hom}$) calculated from the final slip of each fault domain (absolute values in Figure S1). Red stars are the nucleation points of each confined rupture.

## 3.2 Source duration & frequency content

Simulations through the heterogeneous and homogeneous media show increasing differences in source durations and moment rate spectra towards the trench (Fig. 4d to 4f and Figures S2 and S3). The source duration ratio (Duration $_{het}$/ Duration $_{hom}$) is 1.3 in the transitional domain and increases in the shallow domain to 1.6 (Fig. 4a to 4f and Figure S3). These variations translate into corner frequency (*fc*) differences that imply an increasing depletion of high-frequency content trenchwards (Fig. 4). The largest *fc* differences occur in the shallow domain, where *fc* in the heterogeneous model is twice lower than in the homogeneous model. Minor *fc* differences are observed in the transitional domain, while no differences are observed in the regular domain (Fig. 4d to 4f).

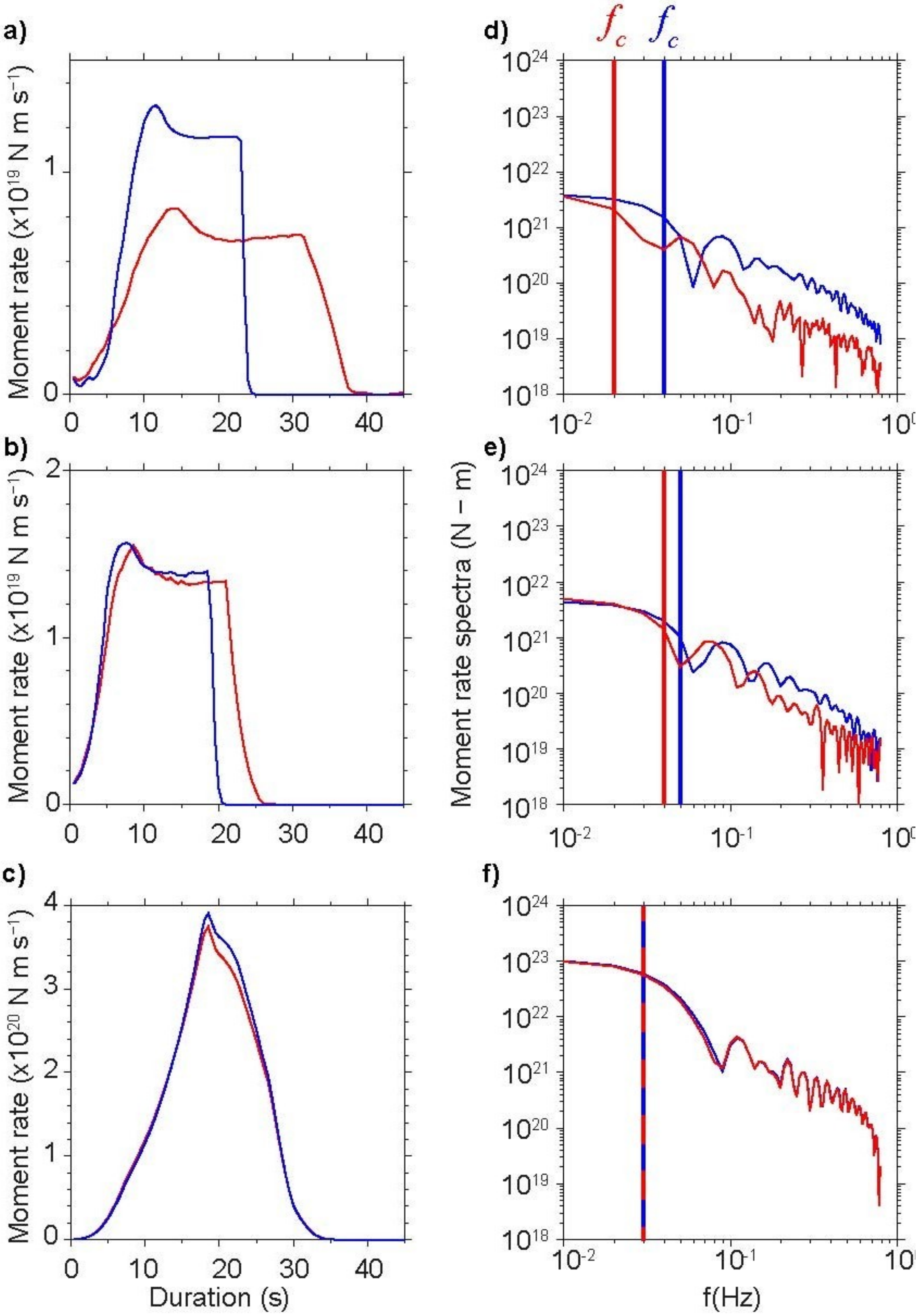


**Figure 4.-** Moment rate of the a) shallow, b) transitional and c) regular domains rupture, and their corresponding moment rate spectra in d), e) and f). Blue and red curves correspond to the results from the homogeneous and heterogeneous model, respectively. $f_c$ is corner frequency.

### 3.3 Rupture speed

To assess rupture speed differences attributed to depth-dependent elastic properties we simulated a continuous rupture throughout the three domains (Fig. 5), and compared the rupture times obtained in both media along a 2D cross section along the center of the fault (Fig. 6d). The nucleation was set at 24 km depth and friction was modified in the shallowmost 3 km of the fault to prevent supershear rupture propagation. We increased $\mu_d$ linearly towards the surface from 0.4 at 10 km depth to 0.8 at the surface (Fig. 5a), resulting in a region with negative stress drop ($\tau_0 < \tau_d$) in the shallowmost 3 km and slip-strengthening ($\mu_d > \mu_s$) in the topmost kilometer (Fig. 5a). Even though this results in reduction of the final slip near the trench (Figure S4) as shown by previous numerical studies (Duan 2012; Galvez et al., 2016), the rupture through the heterogeneous model consistently produces larger slip, particularly in the shallow domain (Fig. 5b and Figure S4). Both ruptures have similar seismic moment (Mw ~ 8.5).

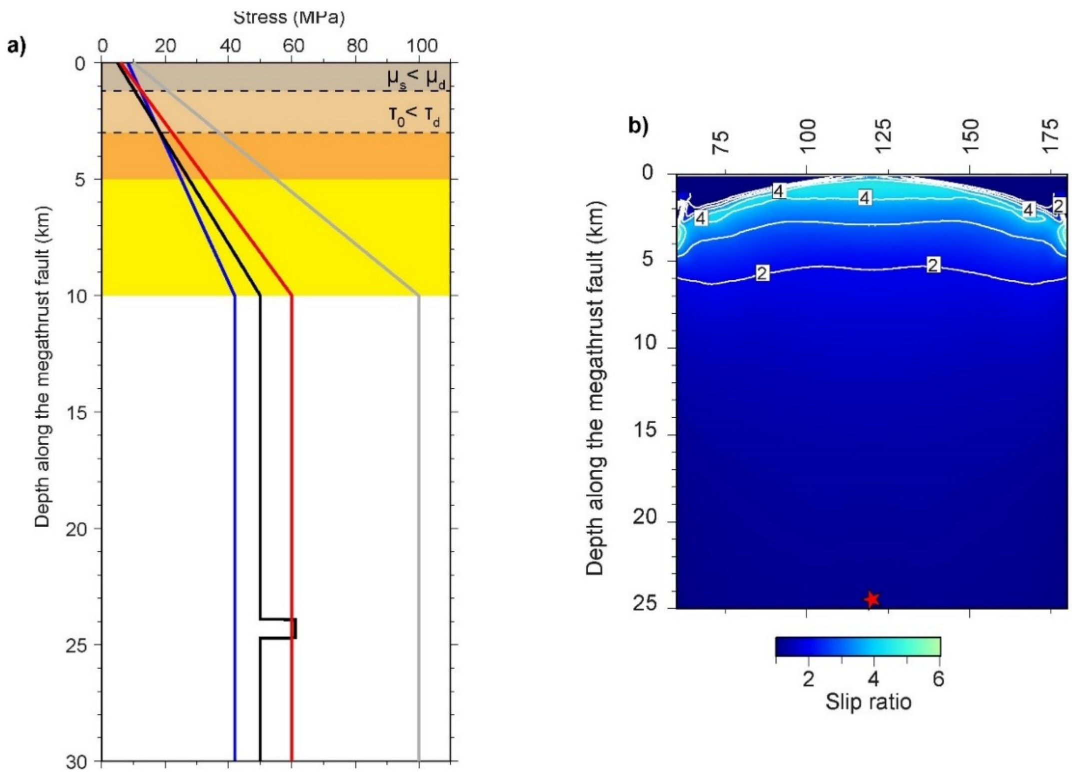


**Figure 5.-** a) Frictional parameters used to simulate the rupture through the entire fault. The blue line is the initial dynamic shear stress, black is the initial shear stress, red curve is the initial shear strength, and gray curve is the initial normal stress. b) Final slip ratio between the heterogeneous and homogenous model ($Slip_{het}/Slip_{hom}$). Red stars is the nucleation points. Final slip values for each elastic model are shown in Figure S4.

The modified frictional setup is enough to suppress supershear propagation in the heterogeneous model, but not in the homogeneous model, where the presence of a small daughter crack rupturing ahead of the main rupture front at supershear speed appears in the shallowmost 6-5 km of the fault (Fig. 6c). This difference may be attributed to the fact that $V_s$, which limits rupture velocity (e.g. Bilek and Lay, 1999), is >1.5 times faster in the shallow domain in the homogeneous scenario than in the heterogeneous, so that rupture acceleration is more effective in the former. To avoid the effect of the daughter crack in the comparison, in the homogeneous model we consider the rupture times only for the main rupture front (Fig.6c). In addition, we spatially smoothed rupture times of the heterogeneous model to suppress the effect of steps generated by the interaction of the rupture with the negative stress drop and slip-strengthening friction at shallow depth (Fig.6d).

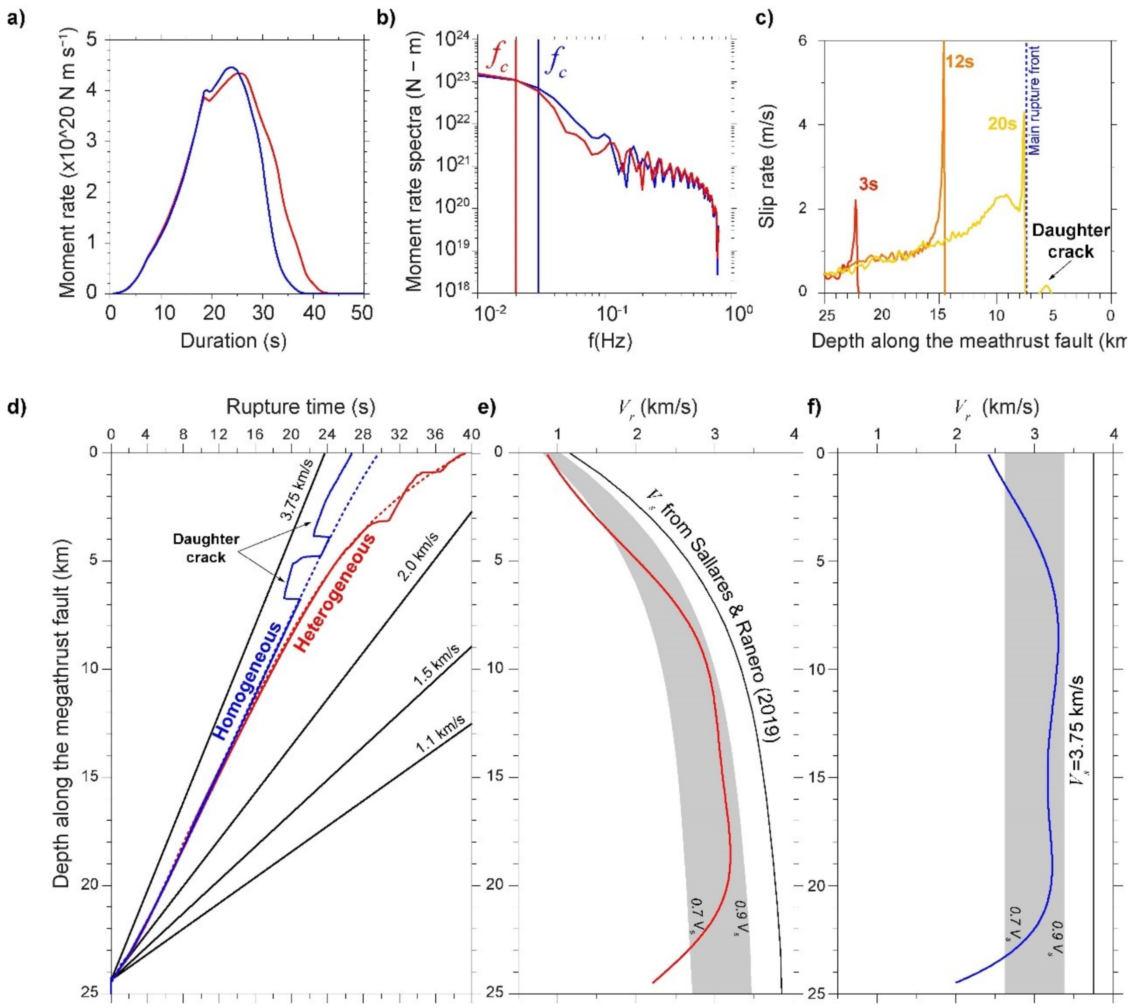


**Figure 6.-** a) Moment rate, and b) moment rate spectra of the rupture through the entire fault. Blue and red lines correspond to results from the heterogeneous and homogeneous model, respectively. c) Slip rate values taken across the center of the fault at 3s, 12s, 20 s of the rupture of the entire fault through the homogenous model. d) Along-dip rupture time depth profile across the center of the fault. Thick blue and red lines are the rupture time profiles for the homogeneous and heterogeneous case, respectively. Dashed blue lines is the rupture time profile of the main rupture front through the homogeneous model derived from slip rate profiles in c). The red dashed line is the smoothed rupture time profile of the heterogeneous model, in which time steps attributed to the negative stress drop and slip-strengthening region are removed. Both dashed lines are used to calculate the normalized rupture time ratio for unit length between both elastic models in Figure 8b. Rupture velocity ($V_r$) curves for the e) heterogeneous and f) homogeneous model. Gray bands show the range of velocity values between 70 % and 90 % of $V_s$ from the medium, which is represented by solid black lines.

Rupture time differences increase trenchwards (dashed colored lines in Fig. 6d). The main rupture front arrives at the trench at 29 s in the homogeneous model and at ~40 s in the heterogeneous models (Fig. 6d), while the total source duration is ~38 s for the homogeneous and ~43 s for the heterogeneous model (Fig 6a). Rupture velocity ($V_r$) derived from rupture time curves show that $V_r$ ranges between 70% and 90% of $V_s$ in both models (Figs. 6e and 6f), consistent with empirical observations (e.g. Bilek and Lay, 1999). Depth-variations of $V_s$ in the heterogeneous model induce similar changes in $V_r$ (Fig. 6e). In both cases, rupture slows down below 70% of $V_s$ in the shallowest ~5 km of the fault, because of the increasing $\mu_d$ assumed in our simulations (Fig. 5a).

### 3.4 Slip rate

We use the simulation results from the rupture through the entire fault in Fig. 5 to explore slip rate differences between both models. Peak slip rate values along a 2D cross section in the center of the fault show increasing differences between elastic models towards the trench (Fig. 7a), where slip velocity is up to 5 times larger in the heterogeneous model. Interestingly, when the rupture reaches the surface, it reflects back resulting in the acceleration of slip rate near the trench (Movie S1). This process, which has been attributed to the contact of the rupture with the free surface in previous numerical studies (e.g. Ma and Beroza, 2008; Huang et al., 2012), occurs in both elastic models, but its effect is larger in the heterogeneous one (right hand side simulation in Movie S1).

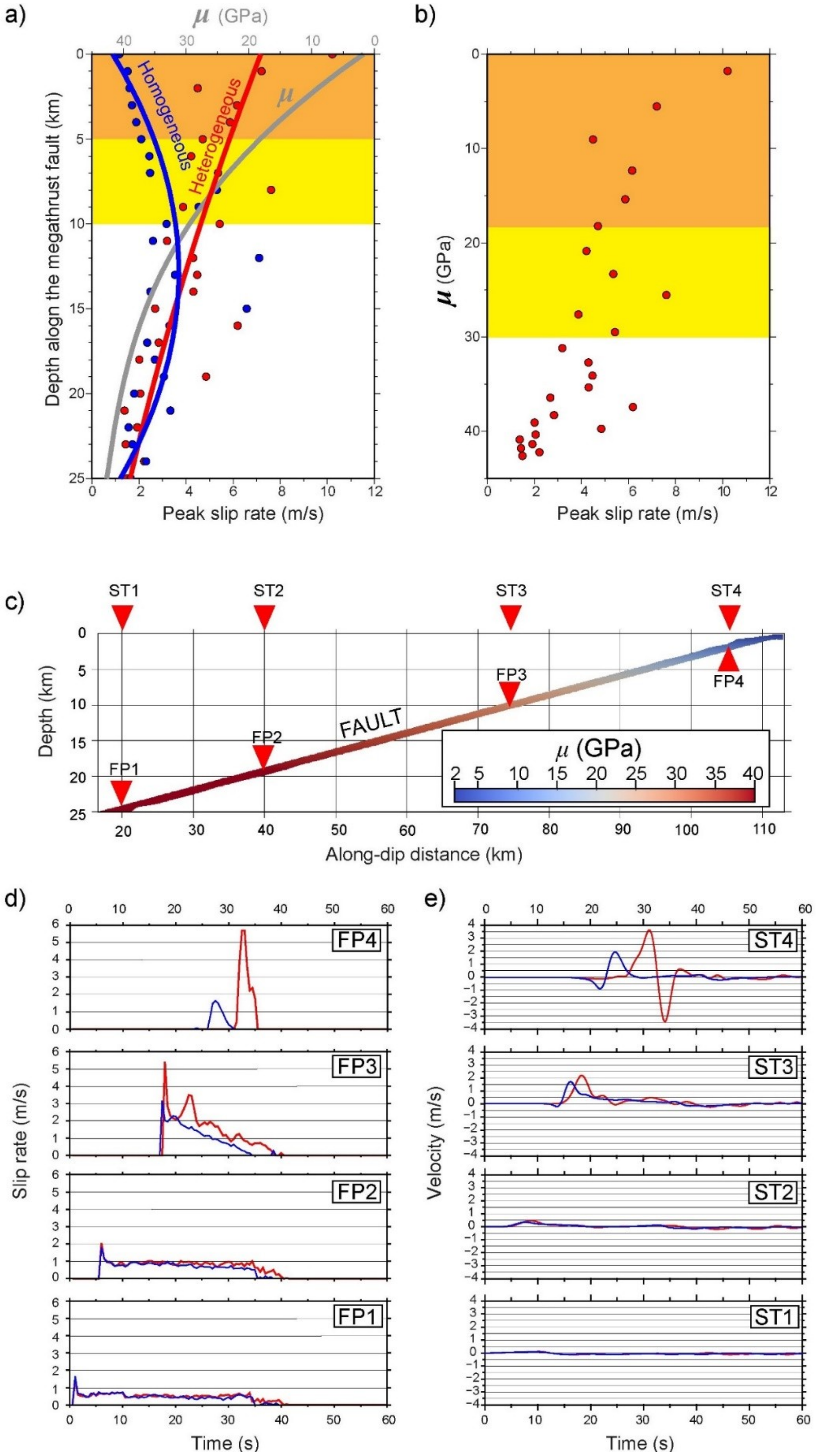


**Figure 7.-** a) Depth profile of the center of the fault showing peak slip rate values of simulations through the entire fault. Blue and red circles are values from the homogeneous and heterogeneous model, respectively. Grey thick line is the depth distribution of rigidity from Sallares and Ranero (2019). b) Same peak slip rate values of the heterogeneous model in a) as a function of rigidity. c) Along-dip profile of the fault showing the location of fault points (FP) and seismic stations (ST) from which slip rate (d) and ground motion (e) values

are measured. The color scale along the fault depicts rigidity of the heterogeneous model.

# 4 Discussion

## 4.1 Depth-varying dynamic rupture properties

The different dynamic rupture properties presented here show a clear depth dependence that arise from variations in elastic properties. The trenchward decrease of rock rigidity enhances slip in the shallow domain, where it is 3 to 10 times larger than in the regular domain, where rigidity is nearly one order of magnitude larger (5 GPa vs 40 GPa; Fig 1g and Fig. 8a). Peak slip rate is also enhanced as rigidity decreases trenchwards (Fig.7b), and effect that is somewhat expected, as peak slip is inversely proportional to $V_s$ and $\rho$ (Ohnaka et al., 1987). Increasing slip rate towards the trench in the heterogeneous model causes stronger ground motion near the trench than in the homogeneous model (Fig. 7c to 7e). Regarding frequency content, corner frequency $f_c$ is up to twice lower in the shallow domain than in the deeper region along the regular domain. This is due to the longer duration of the event in the shallow region, which in turn results from the lower $V_r$. As shown in Fig. 6e and 6f, $V_r$ in our simulations is largely controlled by the depth distribution of $V_s$, which can be up to ~2 times slower in the shallow region than in the regular one (Fig. 6e and 6f). Additional effects slowing down $V_r$ may come from the slip-strengthening behavior of the shallowest megathrust region in our simulations, although at expenses of decreasing slip near the trench (Figure S4). Thus, while fault friction may explain some depth-dependent properties of megathrust earthquakes, it fails to reconcile them all. This aspect is also observed in homogeneous models of the Tohoku-Oki earthquake, which managed to partially explain seismological observations of the event with fault friction variations along the fault, but found inconsistencies in the shallow region, where the amount of high frequency radiated was higher than observed (Huang et al., 2014).

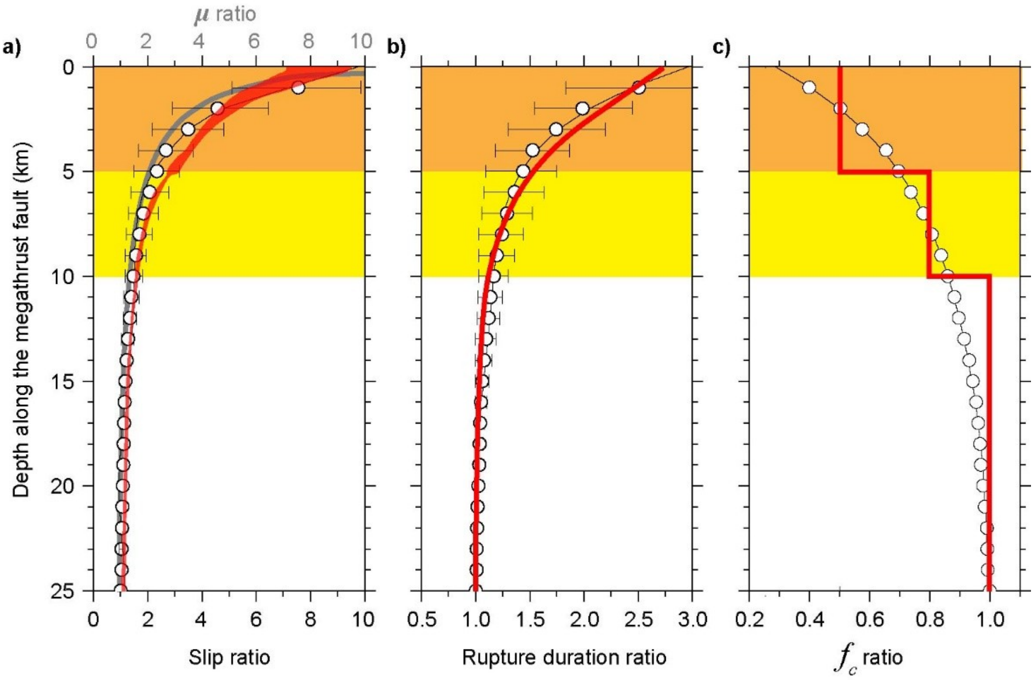


**Figure 8.-** Comparison between depth trends of a) slip ratio, b) rupture duration ratio, and c) $f_c$ ratio from Sallares & Ranero (2019) (white circles) and this study (red). Grey line in a) is rigidity ratio ($\mu_{het}/\mu_{hom}$). Rupture duration ratio (Heterogeneous/Homogeneous) is calculated from rupture time curves in Figure 6d

The depth distribution of slip ratio, rupture time difference per unit length ratio (rupture duration ratio in Fig. 8b) and $f_c$ ratio ($f_{c\ het}/f_{c\ hom}$) calculated in this study quantitatively agree with previous estimates of these properties (Sallares and Ranero, 2019) (Fig. 8). The excellent agreement of the $f_c$ ratio estimates implies that our results are also consistent with the depth-varying Ms-Mw discrepancy presented by the authors, explaining thereby, the depth-dependent megathrust earthquakes source characteristics (Lay et al 2012). We show that large slip, slow rupture and high-frequency depletion are strong indicators of shallow ruptures and thus, potential indicators for high tsunami hazard, in agreement with seismological observations of tsunami earthquakes and larger shallow megathrust earthquakes (e.g. Kanamori and Kikuchi, 1993; Lay and Bilek, 2007; Newman et al.,2011). These results are also consistent with tsunami early warning studies (Lomax and Michelini, 2009; 2011), which reveal that tsunamigenic megathrust earthquakes are related to anomalously long apparent rupture duration (> 50 s) and low P-wave frequency content. However, rather than compliant fault zone sediments (Bilek and Lay, 1999; Polet and Kanamori, 2000), our study strongly suggests that this behavior should be attributed to the decreasing rigidity of rocks in the shallow megathrust, where rigidity decreases one order of magnitude in the shallowmost 5 km of the fault (from ~20 to ~2 GPa; Fig. 1g).

### 4.2 Bimaterial fault

We considered a bimaterial fault interface, including the material contrast between the overriding and downgoing plates, to explore the role that elastic properties at each side of the megathrust fault have in controlling earthquake characteristics. In this simulation, we assume the same 1D distribution of elastic properties from Sallares and Ranero (2019) for the upper plate but a homogeneous media for the downgoing plate (Fig. 9a). To assess slip variations, we simulated three rupture scenarios, each confined to one of the three fault depth ranges. The results show similar slip values to those obtained through the heterogeneous model (Fig. 9b and Figure S5); indicating that slip is mainly controlled by the medium with lower rigidity, which here is the upper plate.

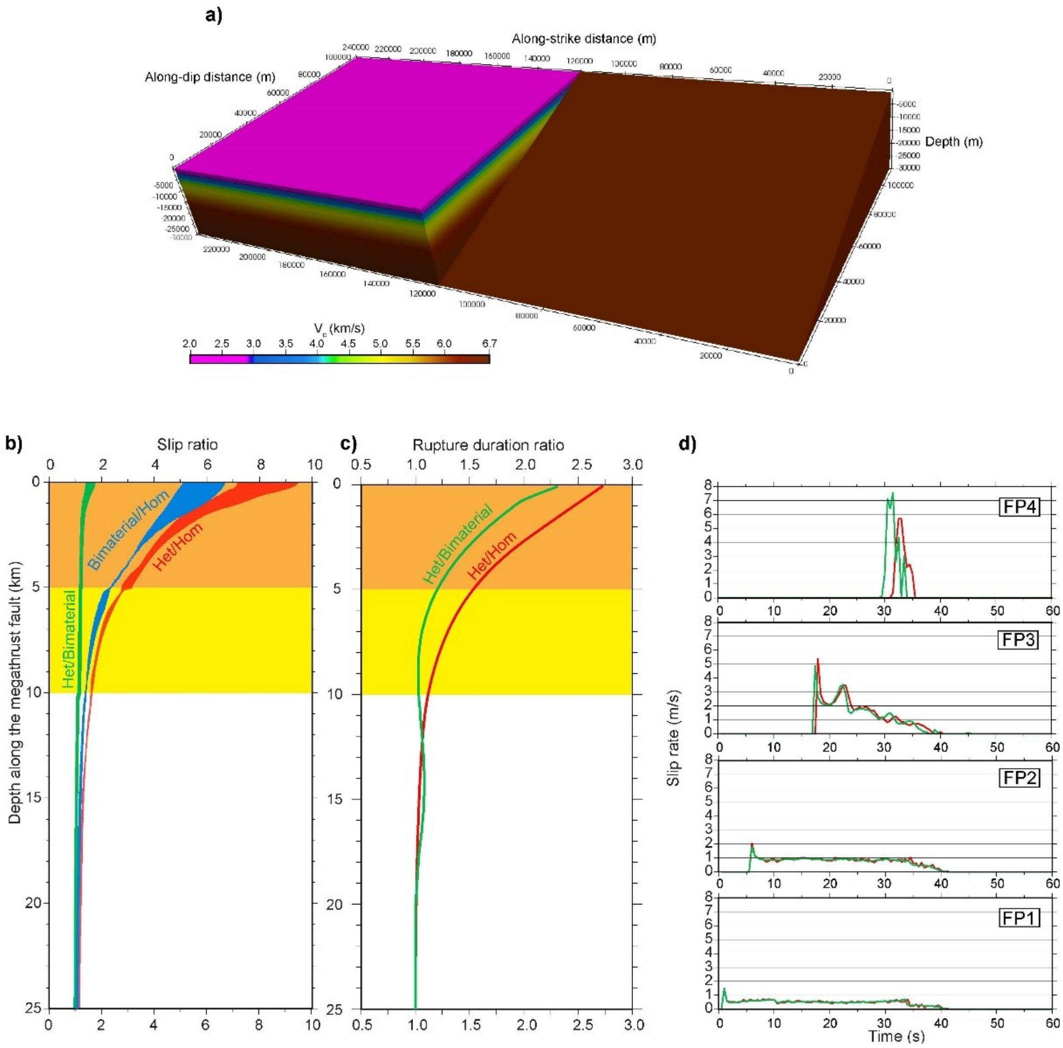


**Figure 9.-** Unstructured mesh showing the $V_p$ distribution of the bimaterial fault. b) Depth trend of slip ratio between the heterogeneous and bimateiral models (green), the bimaterial and homogeneous models (blue), and the heterogeneous and homogeneous models (red). c) Rupture duration ratio between the heterogeneous and bimateiral models (green), and the heterogeneous and homogeneous models (red). d) Slip rate from the bimaterial (green) and the heterogeneous (red) models extracted from fault points 1 to 4 in Figure 7c.

Additionally, we simulate the rupture through the entire fault to assess relative rupture time and slip rate variations between the heterogeneous and the bimaterial case (Fig. 9c and 9d, and Figure S6). We calculated the ratio of rupture time differences per unit of fault length between the heterogeneous and bimaterial models (rupture duration in Fig. 9c and Figure S6 and S7). This ratio shows that rupture duration through the bimaterial model resemble that in the heterogeneous model with some differences along the shallow domain, where the rupture accelerates and propagates at supershear speed in the shallowmost 2 km of the fault. Based on results from the homogeneous model, this effect is possibly attributed to the faster media of the downgoing plate. Using a more compliant and therefore realistic elastic structure of the incoming plate could mitigate this effect. Previous studies focused on bimaterial ruptures indicate that $V_r$ is related to bimaterial contrast and controlled to a greater extent by the lowest $V_s$ (Rubin and Ampuero, 2007; Shlomai et al., 2021). While supershear propagation obscures this relation in the shallow domain, it seems to be the case for the regular and transitional domain, where the rupture duration ratio between the heterogeneous and the bimaterial scenarios is ~1 (Fig. 9c, Figures S6 and S7). Regarding slip rate, the bimaterial model shows larger values than in the heterogeneous model in the shallowmost region of the fault, where the bimaterial contrast is larger (Fig. 9d). This amplification of slip rate, and consequently of ground motion, is consistent with previous bimaterial simulations in which the overlying side of the fault is (i.e. overriding plate) is more compliant than the underlying one (Ma and Beroza, 2008). This mechanism deserves further consideration in numerical simulations as it may have tsunamigenic implications. Although our setup does not have topography, the enhanced slip rate and ground motion occurs at distances of less than 10-15 km from the trench, where the continental slope is commonly found and seafloor may dip 5-15º trenchwards (e.g. Harders et al., 2011). These topographic features, in combination with strong ground shaking, may trigger slope failure processes and contribute to tsunamigenesis (e.g. Tappin et al., 2014).

Overall, results from the bimaterial simulation show a clear depth-dependent behavior of slip, rupture speed and slip rate that is largely controlled by the elastic structure of the softer and slower material of the fault. However, while the distribution used in our simulations is realistic for rocks overlaying the fault, it overestimates elasticity of the incoming plate. The distribution of these properties is often poorly resolved along the entire seismogenic zone. Tomographic models show a more compliant structure of the megathrust in the shallowest region (e.g. Calahorrano et al., 2008; Contreras-Reyes et al., 2017), which could also contribute to enhance slip and slow rupture. Yet, the limited information that we have indicate that variations in seismic velocities occur spatially faster in the downgoing plate along the shallowmost region of the megathrust because of sediment compaction and over-pressured fluid release (Calahorrano et al., 2008). The different seismic structure results from the different tectonic processes acting on both plates. The upper plate is controlled by contractional structures that intensify trenchwards as a result of the convergence (von Huene et al., 1994; Kodaira et al., 2017), while the incoming plate is overlaid by subducting sediments and mostly affected by extensional bending-related faulting (Ranero et al., 2003). These differences and the fact that normal stress is higher on the incoming plate, make the upper plate more compliant than the incoming plate. Therefore, our results strongly support that the elastic properties of rocks overlying the fault in the upper plate control the depth-dependent traits of megathrust earthquakes source properties, as proposed by Sallares and Ranero (2019).

### 4.3 Co-seismic seafloor deformation: implications for tsunamigenesis

Our modeling results also show that the low rigidity of the shallow domain causes large slip near the trench, which in turn enhances large co-seismic seafloor deformation. Rupture simulations in the shallow domain show that uplift ratios ($Uplift_{het}/Uplift_{hom}$) in the shallow domain are up to 4-6 times larger in the heterogeneous model (Fig. 10a) (absolute values are shown in Figure S8). These differences lead to important differences in tsunami amplitudes (Fig.10c and 10d, and Figure S9 and Movie S2 and S3).

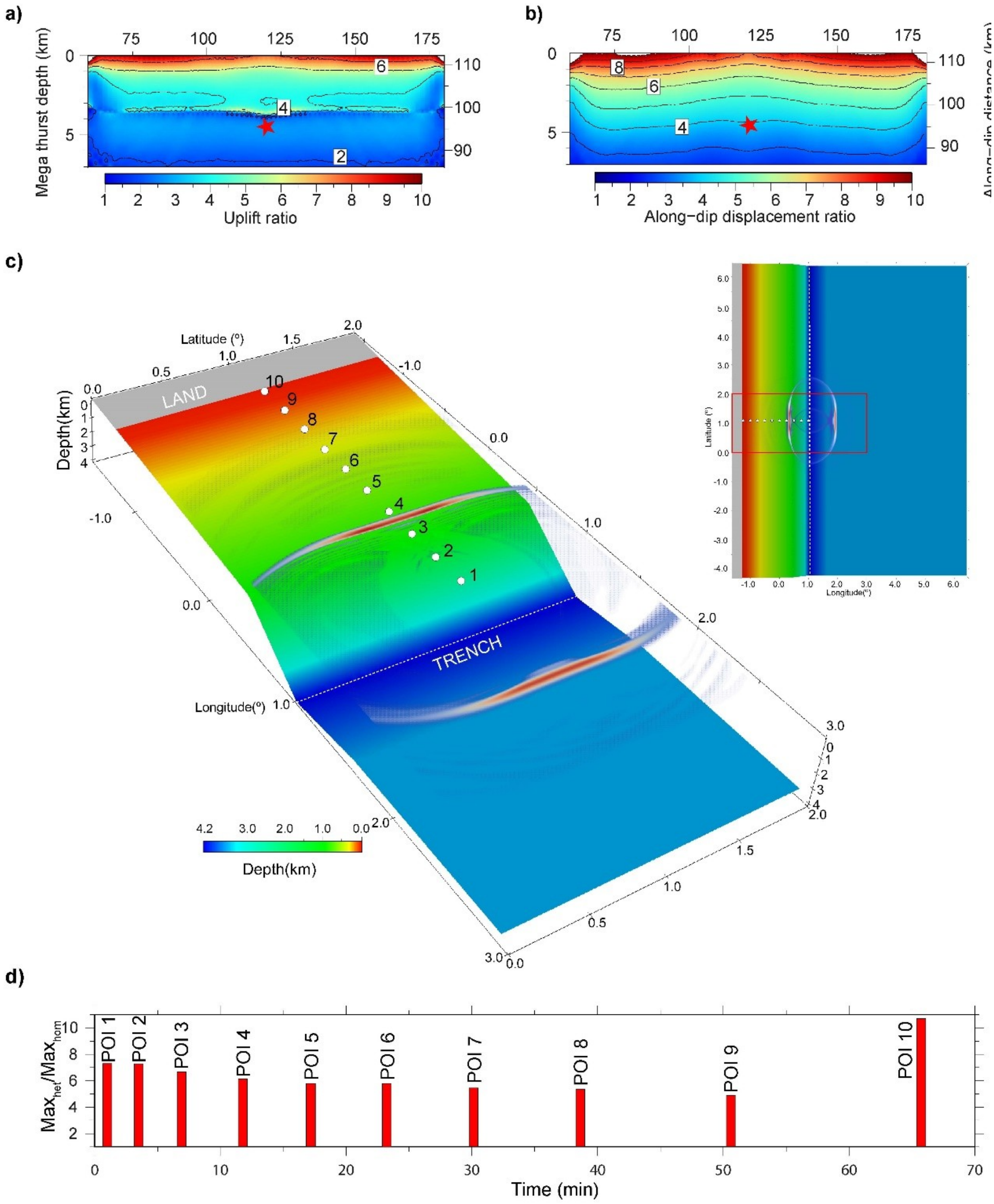


**Figure 10.-** a) Uplift ratio and b) along-dip displacement ratio calculated from the final uplift and along-dip displacement resulting from the rupture through the shallow domain. b) Close-up of the 3D perspective of the bathymetry used as setup (small inset) to simulate the tsunamis associated with the uplift of the shallow domain in the heterogeneous and homogeneous model. Red square in the inset shows the location of the close-up. White dots depict the location of ten points of interest (POI) used to record the temporal evolution of tsunami wave (see Figure S6). c) Maximum tsunami wave ratio versus time calculated for each POI.

We used the final uplift of the shallow domain in both models (Figure S8) and the Tsunami-HySea software (Macías et al., 2017) to calculate the tsunamigenic response. We assume a simplified bathymetry that contains the main topographic features of subduction zones, including the continental shelf and slope, the trench and the outer rise (Fig. 10a). The extent and slopes of each of these domains are based on bathymetry data from the Nicaragua convergent margin (e.g. Sallares et al. 2013). The spatio-temporal evolution of the tsunami wave amplitude was measured at 10 different points of interest (POI) that recorded the tsunami propagation from the trench to the shore (Fig. 10c). Figure 10d shows the maximum wave ratio ($Max_{het}$ /$Max_{hom}$) at each POI, while the absolute values of the tsunami amplitude can be found in the Figure S9. The maximum wave amplitude of the tsunami derived from the heterogeneous model is 6-8 times larger than that from the homogeneous model, and differences increase to ~10 at the shore, because of the interaction of the shallow bathymetry with the tsunami wave. As indicated in real-case tsunami earthquake studies (Satake, 1994; Satake and Tanioka, 1999; Geist and Bilek, 2001), these results demonstrate the importance of taking into account realistic low-rigidity upper-plate values (1 to 10 GPa) in the shallow domain as they determine large slip and important tsunamigenic uplift.

Simulations of the shallow domain also reveal significant differences in co-seismic along-dip displacement between elastic models. Similar to uplift, along-dip displacement ratios (Along-dip $_{het}$/ Along-dip $_{hom}$) increases towards the trench, where displacement may be up to 8-10 times larger in the heterogeneous model (Fig. 10b). Trenchward displacement of the slope region may promote folding of accretionary structures (Tanioka and Seno, 2001), and reactivation of pop-up structures (Hananto et al., 2020), providing additional tsunami sources as indicated in previous simulations (e.g. Murphy et al., 2016).

# 5 Conclusions

We demonstrate that depth-dependent variations of upper-plate elastic properties along the megathrust fault exert a major effect on rupture dynamics and tsunamigenesis. We performed dynamic rupture simulations through a homogeneous and heterogeneous elastic model, and a bimaterial fault. The assumed friction properties are the same in all simulations. We use the depth distribution of $V_p$, $V_s$ and $\rho$ from Sallares and Ranero (2019) to build the heterogeneous scenario, while we assumed the elastic properties of rocks overlying the fault at 25 km of depth to build the homogeneous one.

The results show that decreasing rigidity of the country rock is the main determining factor for enhanced slip, slip rate, slow rupture, and depleted high-frequency energy radiation in the shallow domain, and that fault friction may provide additional controls but to a lesser extent. Depth-dependent elastic properties also affect the dynamics of slip rate. Peak slip rate values in the heterogeneous model anticorrelate with rigidity variations. The increment in peak slip rate correlates with enhanced ground motion in the heterogeneous model, an effect that is amplified if we consider a bimaterial contrast across the fault.

The depth distribution of slip ratio, rupture duration ratio and $f_c$ ratio quantitatively agrees with empirical estimates by Sallares and Ranero (2019), thus explaining most seismological observations regarding the depth-dependent behavior of tsunami earthquakes and large shallow megathrust earthquakes (e.g. Tohoku-Oki). In addition, bimaterial simulations show that slip, rupture velocity and slip rate are largely controlled by the softer side of the fault, which according to geophysical observations is likely to be the upper plate side.

The anomalously large slip in the shallow domain, together with an increasing compliance of the upper plate towards the trench, result in larger co-seismic seafloor deformation than in a homogeneous medium. Uplift differences between elastic models translate into order-of-magnitude differences in tsunami amplitude at the shore. The low rigidity at the toe of the upper plate also enhances along-dip displacement, which may contribute to amplifying the tsunamigenic response.

This study shows the importance of considering realistic variations in megathrust elastic properties and upper-plate rigidity in dynamic rupture simulations and in source models for tsunami modeling. Neglecting these properties may result in significant underestimation of slip, rupture time, local ground motion, seafloor co-seismic deformation and tsunami size, leading to underestimation of the tsunami hazard of the margin.

# Acknowledgments

M. Prada is funded by the Beatriu de Pinós postdoctoral programme of the Government of Catalonia's Secretariat for Universities and Research of the Ministry of Economy and Knowledge (Ref # 2017BP00170). J.P.A. is supported by the Investments in the Future project UCAJEDI (ANR-15-IDEX-01) managed by the French National Research Agency (ANR). We thank Florian Le Pape for his assistance during the generation of the bimaterial unstructured mesh. Dynamic rupture simulations in this study were done at the Super Computer Shaheen II at KAUST University. Shaheen II is a Cray XC40 delivering over 7.2 Pflop/s of theoretical peak performance. Overall, the system has a total of 197,568 processor cores and 790 TB of aggregate memory. Tsunami-HySEA code development is supported by the Spanish Government-FEDER funded project MEGAFLOW (RTI2018-096064-B-C21).

# Open Research

Data were not used, nor created for this research

# References

Bilek, S. L., & Lay, T. (1999). Rigidity variations with depth along interplate megathrust faults in subduction zones. *Nature*, *400*(6743), 443-446.

Byrne, D. E., Davis, D. M., & Sykes, L. R. (1988). Loci and maximum size of thrust earthquakes and the mechanics of the shallow region of subduction zones. *Tectonics*, *7*(4), 833-857.

Calahorrano, A., Sallarès, V., Collot, J. Y., Sage, F., & Ranero, C. R. (2008). Nonlinear variations of the physical properties along the southern Ecuador subduction channel: Results from depth-migrated seismic data. Earth and Planetary Science Letters, 267(3-4), 453-467.

Contreras-Reyes, E., Maksymowicz, A., Lange, D., Grevemeyer, I., Muñoz-Linford, P., & Moscoso, E. (2017). On the relationship between structure, morphology and large coseismic slip: A case study of the Mw 8.8 Maule, Chile 2010 earthquake. *Earth and Planetary Science Letters*, *478*, 27-39.

Day, S. M., Dalguer, L. A., Lapusta, N., & Liu, Y. (2005). Comparison of finite difference and boundary integral solutions to three−dimensional spontaneous rupture. Journal of Geophysical Research: Solid Earth, 110(B12). doi:10.1029/2005JB003813, 2005

Duan, B. (2012). Dynamic rupture of the 2011 Mw 9.0 Tohoku−Oki earthquake: Roles of a possible subducting seamount. *Journal of Geophysical Research: Solid Earth*, *117*(B5).

Galvez, P., Ampuero, J. P., Dalguer, L. A., Somala, S. N., & Nissen-Meyer, T. (2014). Dynamic earthquake rupture modelled with an unstructured 3-D spectral element method applied to the 2011 M 9 Tohoku earthquake. *Geophysical Journal International*, *198*(2), 1222-1240.

Galvez, P., Dalguer, L. A., Ampuero, J. P., & Giardini, D. (2016). Rupture reactivation during the 2011 M w 9.0 Tohoku earthquake: Dynamic rupture and ground−motion simulations. *Bulletin of the Seismological Society of America*, *106*(3), 819-831.

Geersen, J. (2019). Sediment-starved trenches and rough subducting plates are conducive to tsunami earthquakes. *Tectonophysics*, *762*, 28-44.

Geist, E. L., & Bilek, S. L. (2001). Effect of depth−dependent shear modulus on tsunami generation along subduction zones. *Geophysical research letters*, *28*(7), 1315-1318.

Hananto, N. D., Leclerc, F., Li, L., Etchebes, M., Carton, H., Tapponnier, P., ... & Wei, S. (2020). Tsunami earthquakes: Vertical pop-up expulsion at the forefront of subduction megathrust. *Earth and Planetary Science Letters*, *538*, 116197. https://doi.org/10.1016/j.epsl.2020.116197

Harders, R., Ranero, C. R., Weinrebe, W., & Behrmann, J. H. (2011). Submarine slope failures along the convergent continental margin of the Middle America Trench. *Geochemistry, Geophysics, Geosystems*, *12*(6).

Huang, Y., Ampuero, J. P., & Helmberger, D. V. (2016). The potential for supershear earthquakes in damaged fault zones–theory and observations. Earth and Planetary Science Letters, 433, 109-115.

Huang, Y., Ampuero, J. P., & Kanamori, H. (2014). Slip-weakening models of the 2011 Tohoku-Oki earthquake and constraints on stress drop and fracture energy. *Pure and Applied Geophysics*, *171*(10), 2555-2568.

Huang, Y., Meng, L., & Ampuero, J. P. (2012). A dynamic model of the frequency-dependent rupture process of the 2011 Tohoku-Oki earthquake. *Earth, planets and space*, *64*(12), 1061-1066.

Huang, Y., & Ampuero, J. P. (2011). Pulse−like ruptures induced by low−velocity fault zones. *Journal of Geophysical Research: Solid Earth*, *116*(B12).

Hyndman, R. D., Yamano, M., & Oleskevich, D. A. (1997). The seismogenic zone of subduction thrust faults. *Island Arc*, *6*(3), 244-260.

Jeppson, T.N., Tobin, H.J., and Hashimoto, Y., (2018). Laboratory measurements quantifying elastic properties of accretionary wedge sediments: Implications for slip to the trench during the 2011 Mw 9.0 Tohoku-Oki earthquake:Geosphere, v. 14, no. 4, p. 1411–1424, https://doi. org/10.1130/GES01630.1.

Kanamori, H. (1972). Mechanism of tsunami earthquakes. *Physics of the earth and planetary interiors*, *6*(5), 346-359.

Kanamori, H., & Kikuchi, M. (1993). The 1992 Nicaragua earthquake: a slow tsunami earthquake associated with subducted sediments. *Nature*, *361*(6414), 714-716.

Kanamori, H. and K. Yomogida, (2011) Preface. First Results of the 2011 Off the Pacific Coast of Tohoku Earthquake, Earth Planets Space, 63(7), 511, doi:10.5047/eps.2011.07.019.

Kaneko, Y., N. Lapusta, and J.-P. Ampuero (2008), Spectral element modeling of spontaneous earthquake rupture on rate and state faults: Effect of velocity-strengthening friction at shallow depths, J. Geophys. Res., 113, B09317, doi:10.1029/2007JB005553.

Kodaira, S., Nakamura, Y., Yamamoto, Y., Obana, K., Fujie, G., No, T., Kaiho, Y., Sato, T., and Miura, S., 2017, Depth-varying structural characters in the rupture zone of the 2011 Tohoku-oki earthquake: Geosphere, v. 13, no. 5, p. 1408–1424, doi:10.1130/GES01489.1.

Koper, K. D., A. R. Hutko, T. Lay, and O. Sufri (2012), Imaging short- period seismic radiation from the 27 February 2010 Chile (Mw 8.8) earthquake by backprojection of P, PP, and PKIKP waves, J. Geophys. Res., 117, B02308, doi:10.1029/2011JB008576

Lay, T. & Bilek, S. L. (2007). Anomalous earthquake ruptures at shallow depths on subduction zone megathrusts. in The Seismogenic Zone of Subduction Thrust Faults (eds. Dixon, T. & Moore, C.) 476–511, Columbia Univ. Press. https://doi.org/10.7312/dixo13866-015

Lay, T., H. Kanamori, C. J. Ammon, K. D. Koper, A. R. Hutko, L. Ye, H. Yue, and T. M. Rushing (2012), Depth-varying rupture properties of subduction zone megathrust faults, J. Geophys. Res., 117, B04311, doi:10.1029/2011JB009133.

Li, J., Shillington, D. J., Saffer, D. M., Bécel, A., Nedimović, M. R., Kuehn, H., ... & Abers, G. A. (2018). Connections between subducted sediment, pore-fluid pressure, and earthquake behavior along the Alaska megathrust. *Geology*, *46*(4), 299-302. https://doi.org/10.1130/G39557.1

Lomax, A. & Michelini, A., (2009). Tsunami early warning using earthquake rupture duration, Geophys. Res. Lett., 36, L09306, doi:10.1029/2009GL037223.

Lomax, A., & Michelini, A. (2011). Tsunami early warning using earthquake rupture duration and P-wave dominant period: the importance of length and depth of faulting. *Geophysical Journal International*, *185*(1), 283-291.

Lotto, G. C., Dunham, E. M., Jeppson, T. N., & Tobin, H. J. (2017). The effect of compliant prisms on subduction zone earthquakes and tsunamis. *Earth and Planetary Science Letters*, *458*, 213-222. https://doi.org/10.1016/j.epsl.2016.10.050

Ma, S. (2012). A self-consistent mechanism for slow dynamic deformation and tsunami generation for earthquakes in the shallow subduction zone. Geophys. Res. Lett. 39, L11310, http://dx.doi.org/10.1029/2012GL051854.

Ma, S. and G. C. Beroza. (2008) Rupture dynamics on a bimaterial interface for dipping faults, Bull. Seismol. Soc. Am., 98(4), 1642–1658, doi:10.1785/0120070201.

Macías, J., Castro, M. J., Ortega, S., Escalante, C., & González-Vida, J. M. (2017). Performance benchmarking of tsunami-HySEA model for NTHMP's inundation mapping activities. *Pure and Applied Geophysics*, *174*(8), 3147-3183.

McIntosh, K. D., E. A. Silver, I. Ahmed, A. Berhorst, C. R. Ranero, R. K. Kelly, and E. R. Flueh (2007), The Nicaragua convergent margin, in The Seismogenic Zone of Subduction Thrust Faults, Part III, edited by T. H. Dixon and J. C. Moore, chap. 9, pp. 257–287, Columbia Univ. Press, New York.

Meng, L., A. Inbal, and J.-P. Ampuero, (2011). A window into the complexity of the dynamic rupture of the 2011 Mw 9 Tohoku-Oki earthquake, Geophys. Res. Lett., 38, L00G07, doi:10.1029/2011GL048118, 2011.

Moreno, M., Melnick, D., Rosenau, M., Baez, J., Klotz, J., Oncken, O., ... & Hase, H. (2012). Toward understanding tectonic control on the Mw 8.8 2010 Maule Chile earthquake. *Earth and Planetary Science Letters*, *321*, 152-165. doi:10.1016/j.epsl.2012.01.006

Murphy, S., Di Toro, G., Romano, F., Scala, A., Lorito, S., Spagnuolo, E., ... & Nielsen, S. (2018). Tsunamigenic earthquake simulations using experimentally derived friction laws. *Earth and Planetary Science Letters*, *486*, 155-165. https://doi.org/10.1016/j.epsl.2018.01.011

Murphy, S., Scala, A., Herrero, A., Lorito, S., Festa, G., Trasatti, E., ... & Nielsen, S. (2016). Shallow slip amplification and enhanced tsunami hazard unravelled by dynamic simulations of mega-thrust earthquakes. Scientific reports, 6(1), 1-12.

Newman, A. V., G. Hayes, Y. Wei, and J. Convers (2011), The 25 October 2010 Mentawai tsunami earthquake, from real-time discriminants, finite-fault rupture, and tsunami excitation, Geophys. Res. Lett., 38, L05302, doi:10.1029/2010GL046498.

Ohnaka, M., Kuwahara, Y., & Yamamoto, K. (1987). Constitutive relations between dynamic physical parameters near a tip of the propagating slip zone during stick-slip shear failure. Tectonophysics, 144(1-3), 109-125.

Peter, D., D. Komatitsch, Y. Luo, R. Martin, N. Le Goff, E. Casarotti, P. Le Loher, F. Magnoni, Q. Liu, C. Blitz, et al. (2011). Forward and adjoint simulations of seismic wave propagation on fully unstructured hexahedral meshes, Geophys. J. Int. 186, 721–739.

Polet, J., and H. Kanamori (2000), Shallow subduction zone earthquakes and their tsunamigenic potential, Geophys. J. Int., 142, 684–702, doi:10.1046/j.1365-246x.2000.00205.x.

Ranero, C. R., Morgan, J. P., McIntosh, K., & Reichert, C. (2003). Bending-related faulting and mantle serpentinization at the Middle America trench. *Nature*, *425*(6956), 367-373.

Rubin, A. M., & Ampuero, J. P. (2007). Aftershock asymmetry on a bimaterial interface. Journal of Geophysical Research: Solid Earth, 112(B5).

Sallarès, V., Melendez, A., Prada, M., Ranero, C. R., McIntosh, K., & Grevemeyer, I. (2013). Overriding plate structure of the Nicaragua convergent margin: Relationship to the seismogenic zone of the 1992 tsunami earthquake. *Geochemistry, Geophysics, Geosystems*, *14*(9), 3436-3461. doi:10.1002/ggge.20214.

Sallarès, V., & Ranero, C. R. (2019). Upper-plate rigidity determines depth-varying rupture behaviour of megathrust earthquakes. *Nature*, *576*(7785), 96-101. https://doi.org/10.1038/s41586-019-1784-0

Satake, K. (1994), Mechanism of the 1992 Nicaragua tsunami earthquake, Geophys. Res. Lett., 21, 2519–2522, doi:10.1029/94GL02338.

Satake, K., and Y. Tanioka (1999), Sources of tsunami and tsunamigenic earthquakes in subduction zones, Pure Appl. Geophys., 154, 467 – 483.

Scholz, C. (1998), Earthquakes and friction laws, Nature, 391, 37 – 42.

Shlomai, H., Kammer, D. S., Adda-Bedia, M., Arias, R. E., & Fineberg, J. (2021). Unstable cracks trigger asymptotic rupture modes in bimaterial friction. Journal of the Mechanics and Physics of Solids, 149, 104330.

Simons, M., Minson, S. E., Sladen, A., Ortega, F., Jiang, J., Owen, S. E., ... & Webb, F. H. (2011). The 2011 magnitude 9.0 Tohoku-Oki earthquake: Mosaicking the megathrust from seconds to centuries. *science*, *332*(6036), 1421-1425. doi:10.1126/science.1206731

Tanioka, Y., and T. Seno (2001), The sediment effect on tsunami generation of the 1896 Sanriku tsunami earthquake, Geophys. Res. Lett., 28, 3389 – 3392.

Tappin, D.R., Grilli, S.T., Harris, J.C., Geller, R.J., Masterlark, T., Kirby, J.T., Shi, F., Ma, G., Thingbaijam, K.K.S., Mai, P.M., 2014. Did a submarine landslide contribute to the 2011 Tohoku tsunami? Mar. Geol. 357, 344–361. https://doi.org/10.1016/j.margeo.2014.09.043

Tobin, H. J., & Saffer, D. M. (2009). Elevated fluid pressure and extreme mechanical weakness of a plate boundary thrust, Nankai Trough subduction zone. *Geology*, *37*(8), 679-682.

van Zelst, I., Wollherr, S., Gabriel, A.‐A., Madden, E. H., & van Dinther, Y. (2019). Modeling megathrust earthquakes across scales: one‐way coupling from geodynamics and seismic cycles to dynamic rupture. Journal of Geophysical Research: Solid Earth, 124, 11,414–11,446. https://doi.org/10.1029/ 2019JB017539

von Huene, R., Klaeschen, D., Cropp, B., and Miller, J., 1994, Tectonic structure across the accretionary and erosional parts of the Japan Trench margin: Journal of Geophysical Research, v. 99, p. 22,349–22,361, doi: 10 .1029 /94JB01198